Energy materials

A high-performance pseudocapacitive electrode based on CuO–MnO$_2$ composite in redox-mediated electrolyte

Manas Mandal[1,2], Radha Nagaraj[3], Krishna Chattopadhyay[4], Malay Chakraborty[2], Sujit Chatterjee[2], Debasis Ghosh[3], and Swapan Kumar Bhattacharya[2,*]

[1] *Department of Chemistry, Sree Chaitanya College, Habra, 24 Parganas (N), Habra 743268, West Bengal, India*
[2] *Physical Chemistry Section, Department of Chemistry, Jadavpur University, Kolkata 700032, West Bengal, India*
[3] *Centre for Nano & Material Sciences, Jain Global Campus, JAIN University, Bangalore 562112, India*
[4] *School of Chemical Sciences, Indian Association for the Cultivation of Science, Kolkata 700032, West Bengal, India*

ABSTRACT

In the present work, a simple and cost-effective precipitation approach was carried out to fabricate CuO nano-needle, and its electrochemical performance was evaluated in a redox-mediated electrolyte (2 M KOH and 0.3 M K$_3$Fe(CN)$_6$). A high specific capacitance of 2519 F/g was recorded at a specific current of 8 A/g. However, the electrode suffered from poor rate capability as the specific capacitance was rapidly decreased to 100 and 1 F/g when the specific current was increased to 30 and 50 A/g, respectively. The CuO nanoparticles were further modified with MnO$_2$ by a hydrothermal method, and the resulting CuO–MnO$_2$ (CMO6) electrode delivered a high specific capacitance of 539 F/g even at very high specific current of 50 A/g. The as-synthesized electrode materials were structurally and morphologically characterized using X-ray diffraction (XRD) analysis, Fourier transform infrared spectroscopy (FTIR), X-ray photoelectron spectroscopy (XPS), scanning electron microscopy (SEM), and transmission electron microscopy (TEM). The electrochemical performances of the CuO and MnO$_2$–CuO composites have been examined in detail.

🍂 Springer

GRAPHIC ABSTRACT

Synopsis Modification of pristine CuO nano-needles with MnO$_2$ nanosheets improved the electrochemical performance of the material. The composite was able to deliver a high specific capacitance of 539 F/g even at very high specific current of 50 A/g.
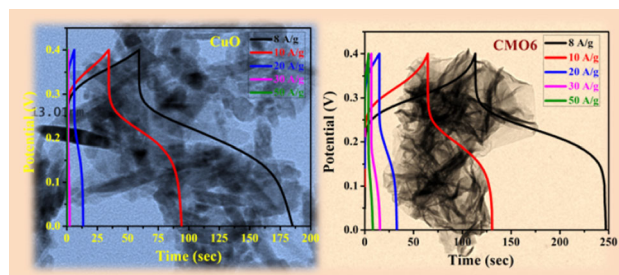
Introduction

Enormous energy consumption by our electronically biased modern daily life triggers the scientists to search for a sustainable and renewable energy resource for future energy storage. Solar and wind energies have drawn global attention as renewable sources of energy, but their uncertain and discontinuous nature makes them unreliable [1]. Recently, electrochemical capacitors, also known as ultracapacitor or supercapacitors (SCs), have attracted remarkable attention in light of their unique properties of high power density, moderate energy density, long cycle life, fast charging capacity and green environmental protection [2, 3]. Based on the charge storage mechanism, SCs are classified into two pure types besides the hybrid one: (i) electrical double-layer capacitors (EDLCs) and (ii) pseudocapacitors. In EDLCs, the capacitance originates due to charge accumulation at the interfaces between electrode surface and electrolyte. The carbonaceous materials such as graphene and carbon nanotubes (CNTs) show such type of double-layer capacitance [4]. On the other hand, pseudocapacitance comes from the fast Faradaic redox reactions between electrode materials and electrolyte ions. Due to multiple oxidation states of the transition metals, its oxides, hydroxides and sulfides are commonly chosen as the pseudocapacitive electrode materials [5–8]. To

enhance the efficiency of the electrode materials, the idea of incorporating combinatorial transition metal oxides with multiple electroactive redox sites has been developing. Not only the choice of electrode materials but also the surface architectures of the material, electrolyte, separator, etc. can alter the efficiency of supercapacitor. Recently, in terms of modification of electrolyte, the addition of a foreign redox system into the mother electrolyte solution as an additional source of pseudocapacitance is being taken into consideration.

CuO–MnO$_2$ is a well-known composite, which is previously reported for various applications like supercapacitors [2, 3, 9–12], Li-ion batteries [13, 14], heterogeneous catalysts [15–19], sensors [20, 21], etc. However, to the best of our knowledge this work is the first report on supercapacitor application of CuO–MnO$_2$ composite using redox-mediated electrolyte. Herein, pristine CuO and MnO$_2$ nanosheet-wrapped CuO nano-needles were synthesized by the precipitation method followed by a simple and facile hydrothermal technique, and the electrochemical properties were studied in terms of cyclic voltammetry (CV), galvanostatic charge–discharge (GCD) curve and electrochemical impedance spectra (EIS) in redox couple, $[Fe(CN)_6]^{3-}/[Fe(CN)_6]^{4-}$-mediated aqueous electrolyte.

Experimental section

Materials and reagents

Copper(II) nitrate trihydrate, potassium hexacyano-ferrate(III), sodium hydroxide, potassium permanganate were supplied by Merck, India. All the reagents were directly used for the experiment without doing any purification.

Synthesis of CuO

A large number of synthetic routes have been developed for the preparation of CuO with different morphologies [2, 3, 9–11]. Herein, the co-precipitation method was followed for the synthesis of CuO [22]. Briefly, 30 mL 0.1 M aqueous $Cu(NO_3)_2 \cdot 3H_2O$ solution was added dropwise in 20 mL 0.1 M aqueous $K_3[Fe(CN)_6]$ solution with a continuous stirring. The tawny brown colored precipitate of $Cu_3[Fe(CN)_6]_2$ was formed immediately. After one-hour continuous stirring, the solution was kept for 12 h in undisturbed condition. Then, 1 M NaOH was added dropwise to the mixture with a continuous stirring. The prompt color change from tawny brown to deep brown was recognized. The obtained solid product was washed with water for several times and dried at 60 °C in hot air oven.

Synthesis of CuO–MnO₂ composites

A set of two solutions was prepared, each by dispersing 35 mg of as-prepared CuO in 35 mL 0.025 M aqueous solution of $KMnO_4$. Then, the solutions were transferred in two 50 mL stainless steel autoclaves and were kept in the furnace at 180 °C for 3 and 6 h, respectively. After cooling at room temperature, the solid brown products obtained from the two solutions were carefully washed in succession with water and absolute alcohol for several times. The desired materials were obtained after drying at 60 °C for 12 h, and the two products were labeled as CMO3 and CMO6, respectively. The same procedure without the addition of pure CuO was followed for the preparation of pure MnO_2.

Material characterization

The chemical and structural analyses of the as-prepared electrode materials were carried out by X-ray diffraction (XRD, Rigaku ULTIMA-III X-ray diffractometer with Cu Kα radiation (λ = 1.548 Å) analysis, Fourier transform infrared (FTIR, NEXUS 870 Thermo-Nicolet) spectroscopy, and X-ray photoelectron spectroscopy (XPS, using a PHI 5000 Versa Probe II XPS analyzer with a monochromatic Al Kα X-ray source (hν = 1486.71 eV)). From the field emission scanning electron microscopy (FESEM, Carl Zeiss-SUPRA 40) and tunneling electron microscopy (TEM, TECNAI G2-20S-TWIN) images, the surface morphology of the electrode materials was investigated. The surface area of the material was determined by the N_2 adsorption–desorption isotherm.

Electrochemical measurements were taken using a computer-controlled electrochemical working station (Biologic SP 150 and Autolab potentiostat) with a conventional three-electrode electrochemical cell in 2 M KOH aqueous solution containing 0.3 M $K_3[Fe(CN)_6]$. The working electrode was prepared on Ni foam. A platinum plate and a saturated calomel electrode (SCE) were used as counter electrode and reference electrode, respectively. The electrochemical behavior was analyzed in terms of cyclic voltammetry (CV), galvanostatic charge–discharge (GCD) curve and electrochemical impedance spectra (EIS). The specific capacitance of the electrode materials was calculated from CV and GCD measurements using Eqs. 1 and 2, respectively [23].

$$C_s = \frac{\int_{V2}^{V1} i(V)\mathrm{d}V}{2(V2 - V1)vm} \tag{1}$$

$$C_s = \frac{i \times \Delta t}{m \times \Delta V}, \tag{2}$$

where $\int_{V2}^{V1} i(V)\mathrm{d}V$ is the area of the CV curve, $\Delta V = (V2 - V1)$ is the potential window (V), v is the scan rate (mV/s) and m is the mass (g) of the active materials, i is the applied current (A), and Δt is the discharge time (s).

Results and discussion

The synthesis procedure involves two-step chemical reactions: first a quick precipitation of copper hexacyanoferrate [CuHCFe] (co-precipitation method) and then the decomposition of CuHCFe complex in
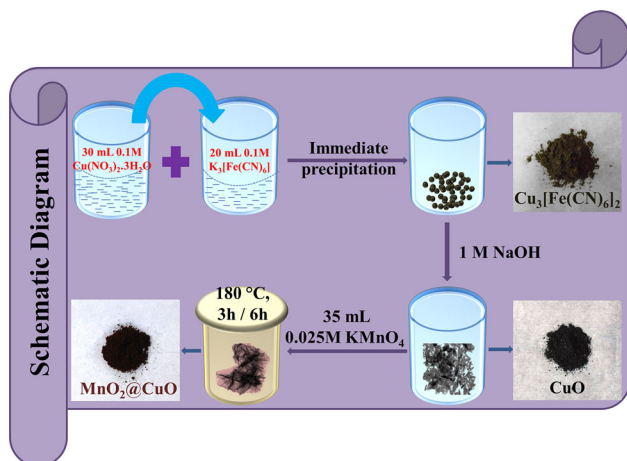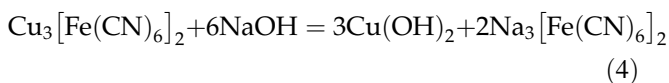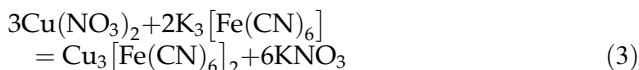
**Scheme 1** Synthetic procedure of CuO–MnO$_2$ composites.
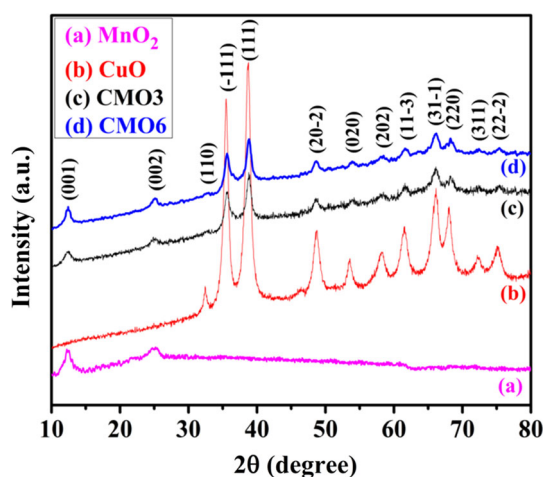
Figure 1 XRD patterns of as-prepared pure MnO$_2$ (a), CuO (b), CMO3 (c) and CMO6 (d) composites.

alkaline medium [24]. The chemical reactions associated with the synthesis procedure are as follows.

$$3Cu(NO_3)_2 + 2K_3\left[Fe(CN)_6\right] = Cu_3\left[Fe(CN)_6\right]_2 + 6KNO_3 \quad (3)$$

$$Cu_3\left[Fe(CN)_6\right]_2 + 6NaOH = 3Cu(OH)_2 + 2Na_3\left[Fe(CN)_6\right]_2 \quad (4)$$

$$Cu(OH)_2 = CuO + H_2O \quad (5)$$

The MnO$_2$ nanosheets are formed from self-decomposition of KMnO$_4$ during hydrothermal reaction [25]. The total synthesis procedure is schematically represented in Scheme 1.

The XRD patterns were taken to determine the phase composition of pure MnO$_2$, CuO and CMO composites as shown in Fig. 1. For pure CuO, the
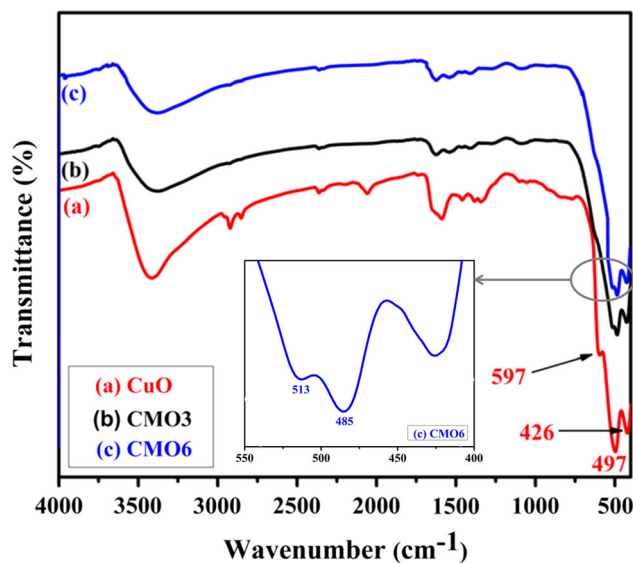

Figure 2 FTIR spectra of as-prepared pure CuO (a), CMO3 (b) and CMO6 (c) composites.

peaks at 2θ (°) of 32.4, 35.5, 38.7, 48.7, 53.5, 58.3, 61.5, 66, 68, 72.3, and 75.1 correspond to (110), (− 111), (111), (20 − 2), (020), (202), (11 − 3), (31 − 1), (220), (311), and (22 − 2) planes of face-centered cubic crystal. All the peaks are well matched with JCPDS Card No: 05-0661 (Tenorite, Syn). The precursor of the CuO is copper hexacyanoferrate, which is confirmed by the XRD pattern as shown in Figure S1(a). For the composites, all the peaks of CuO are present along with the two basal reflections of (001) and (002) at 12.5 and 24.7 peaks for MnO$_2$, which are also present in case of pure MnO$_2$ (Fig. 1a). The peaks of the composites are less intense than the pure CuO as the MnO$_2$ nanosheets wrap around the CuO nanoneedles. Furthermore, the characteristic peaks of MnO$_2$ were more prominent in CMO6.

To investigate the chemical and structural properties, FTIR analysis was carried out and the results are shown in Fig. 2. Pressed KBr pellets of CuO and the composites (CMO3 and CMO6) were used to execute FTIR analysis by NEXUS 870 FTIR (Thermo Nicolet) instrument. The three main characteristic peaks of CuO were observed at 597, 497 and 426 cm^{-1} for A$_u$, B$_u$ and B$_u$ modes, respectively, which confirms the formation of CuO nano-needles. The Cu–O stretching values along (− 101) and (101) directions demonstrate the absorption peaks at 597 and 497 cm^{-1}, respectively [26–29]. The broad absorption peaks between 1300 and 4000 cm^{-1} are ascribed as chemisorbed and/or physisorbed H$_2$O and CO$_2$ molecules

Figure 3 XPS spectra of CMO6 composite: **a** Cu 2p spectrum and **b** Mn 2p spectrum.
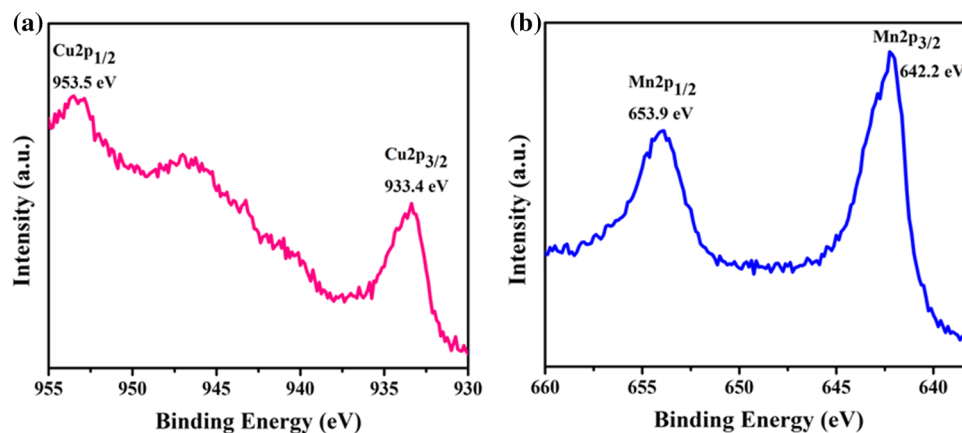

[29, 30]. Moreover, there is no peak in between 610 and 660 cm^{-1} indicating the absence of any other phases like Cu_2O, which appears at 615 cm^{-1} [31]. In both the composites, the two main characteristic peaks are observed at 513 and 485 cm^{-1} corresponding to Mn–O stretching modes in octahedral environment [32]. The peak at 1385 cm^{-1} appears due to the coordination of Mn by O–H [32].

For the chemical analysis of the composite, XPS was carried out, which is shown in Fig. 3. The XPS spectra were accomplished by taking the reference peaks of C1s at 284.2 eV. For the Cu2p in CuO, the two major peaks of Cu2p1/2 and Cu2p3/2 are found at 953.5 and 933.5 eV, respectively, indicating the presence of CuO in composite [16]. Figure 3b shows XPS spectrum for Mn2p; the two peaks at 653.9 and 642.2 eV are attributed to the Mn2p1/2 and Mn2p3/2, respectively, with spin energy difference of 11.7 eV [33].

Figure 4 presents the corresponding FESEM images of as-synthesized CuO and CMO6 composites. It can be seen that the CuO particles are having nano-needle-like structure of length 80–100 nm. Copper hexacyanoferrate, the precursor of CuO nano-needle, consists of small nanoparticles as shown in Figure S1(b). The FESEM image of CMO3 is shown in Figure S2, which indicates the CuO nano-needles are covered up with MnO_2 nanosheets. However, for CMO6 composite, the CuO nanorods are fully wrapped by MnO_2 nanosheets (Fig. 4c), possibly due to longer time of growth. The element mapping images (Fig. 4d–f) confirm the presence of Cu, Mn and O implying the formation of CuO–MnO_2 composite. The TEM images of CuO and CMO6 composites are shown in Fig. 5. The nano-needle structures of CuO were again supported by the TEM images shown in Fig. 5a–c. The length and width of each CuO nano-needle is of 80–100 nm and 10–15 nm, respectively. The TEM images of the CMO6 composite are shown in Fig. 5d, e having different magnifications. Figure 5d, e denotes that the CuO nano-needles were entirely wrapped by MnO_2 nanosheets in CMO6. The energy-dispersive X-ray (EDAX) analysis spectrum (Fig. 5f) also confirms the presence of CuO in the composite.

The surface area plays a crucial role in determining the efficiency of a material as an adsorbent or electrode material. The N_2 adsorption–desorption
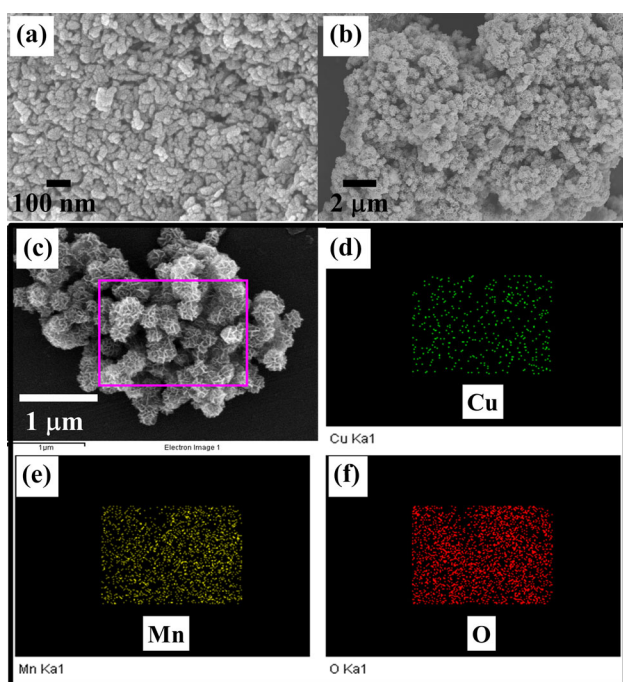
Figure 4 FESEM images of as-prepared pure CuO (**a**) and CMO6 composites (**b**). Mapping images of CMO6 composite (**c–f**).
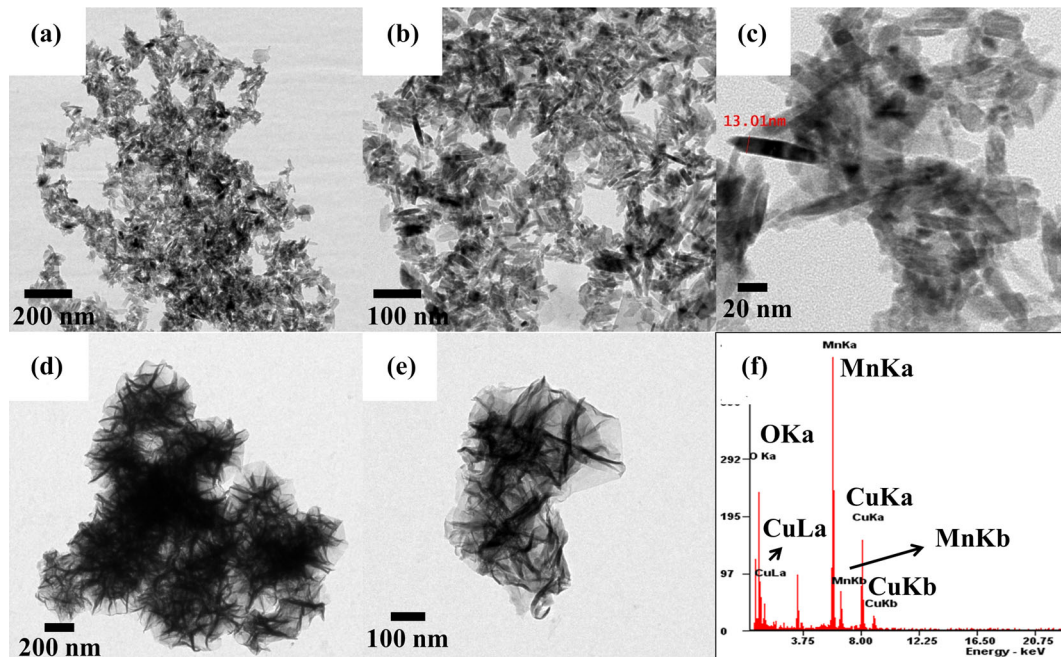
Figure 5 TEM images of as-prepared pure CuO (**a–c**) and CMO6 composite (**d, e**) with different magnification. EDAX spectrum of the CMO6 composite (**f**).

isotherms and Barrett–Joyner–Halenda (BJH) profiles confirm higher surface area and enhanced porosity in the composites in comparison with the pure CuO nano-needles. The surface area of the pure CuO, CMO3 and CMO6 composites was obtained to be 60.43, 66.984 and 78.846 m^2/g, respectively, as measured by the Brunauer–Emmett–Teller (BET) method. The BJH pore size distribution profile (Figs. 6c, d and S3b) shows perfectly monomodal distribution with the maxima of 7.73, 1.96 and 1.79 nm for CuO nano-needle, CMO6 and CMO3 composites, respectively. According to the International Union of Pure and Applied Chemistry (IUPAC), all the BET isotherms show type-4 isotherm with a H3 hysteresis loop. The highly porous nature of the composites appears due to the presence of highly mesoporous and ultrafine MnO$_2$ nanosheets, which results in high electrochemical capacity of the nanocomposite (vide infra).

After fabrication of the working electrode, the electrochemical characterizations were carried out in terms of cyclic voltammetry (CV), galvanostatic charge–discharge (GCD) and electrochemical impedance spectroscopy (EIS). The CV curves of CuO and CMO6 composites at various scan rates in 2 M KOH electrolyte solution containing 0.3 M K$_3$[Fe(CN)$_6$] are shown in Fig. 7a, b, respectively. Both the CV curves show very high value of current, indicating the high

activity of the redox electrolyte. The comparison of CV curves of all the as-synthesized materials at 10 mV/s is shown in Fig. 7c. The high area of the CV curve of CMO6 indicates higher capacitance of the composite than pure CuO and CMO3 composites. The redox-active electrolyte surpluses electron density in conventional electrolyte, improving the ionic conductivity of the electrolyte and enhances the charge storage properties. Furthermore, the shift of the oxidation and reduction potential peaks with an increasing scan rate indicates the quasi-reversible nature of the pseudocapacitive electrode materials in the presence of the redox-active electrolyte. The oxidation peak among the pair of redox peaks in the CV curves appears due to the charging process, involving the conversion of K$_4$[Fe(CN)$_6$] to K$_3$[Fe(CN)$_6$], whereas the reduction peak involves the reverse reaction. The specific capacitance of 7521, 1839, 1051, 872, 745 and 615 F/g was calculated for CMO6 electrode at the scan rate of 1, 10, 20, 50, 100 and 200 mV/s, respectively. But the pristine CuO achieved the capacitance of 7363, 1239, 757, 381, 219 and 125 F/g at the scan rate of 1, 10, 20, 50, 100 and 200 mV/s, respectively. Furthermore, the CMO3 composite shows the specific capacitance of 5354, 1021.5, 686, 391, 244.8 and 152 F/g at the scan rate of 1, 10, 20, 50, 100 and 200 mV/s, respectively. One interesting
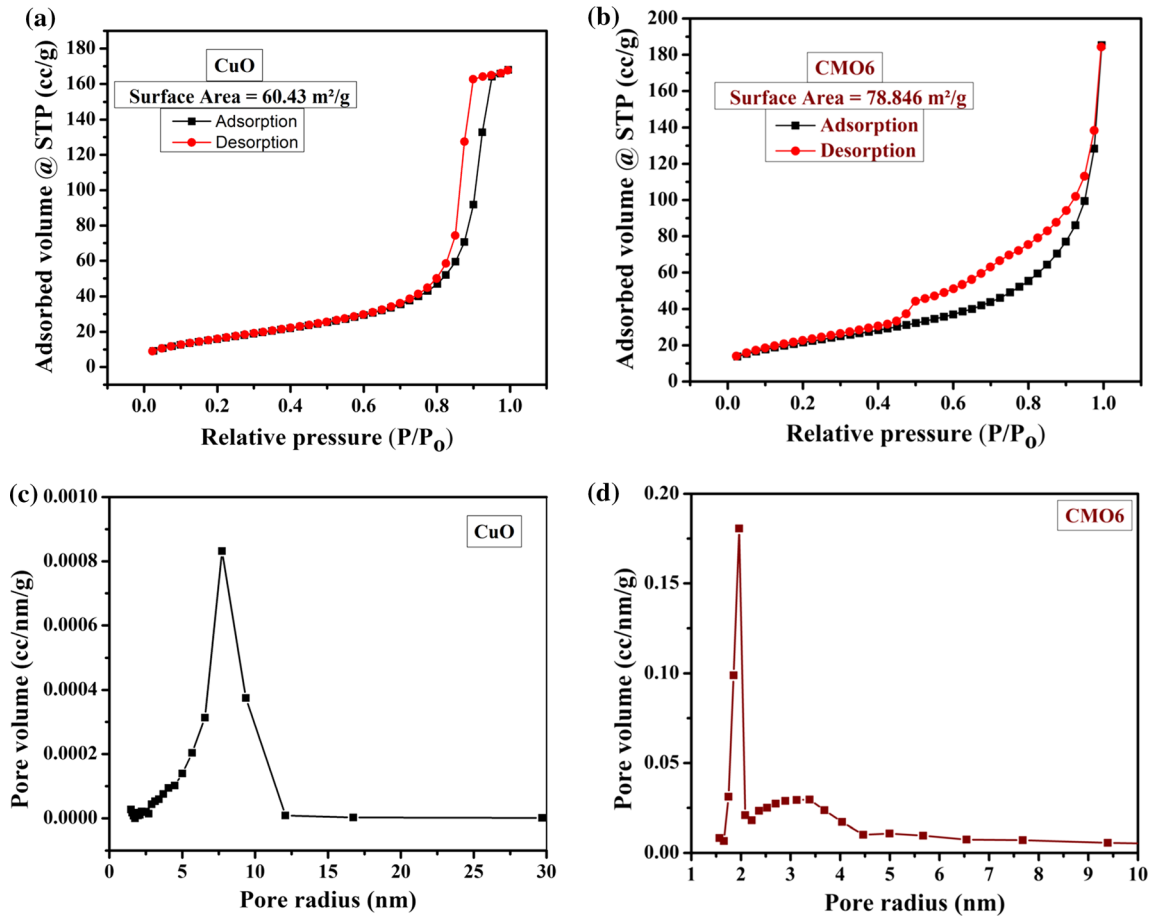
Figure 6 N$_2$ adsorption–desorption isotherms of CuO (**a**) and CMO6 composite (**b**); BJH pore size distribution profile of CuO (**c**) and CMO6 composite (**d**).

point is that the pristine CuO exhibited better electrochemical performance at a low scan rate than at a high scan rate. This may be due to lower rate capability of CuO electrode. The CMO6 composite having high rate capability shows better performance throughout the whole range of scan rate. At the higher scan rate, the electrolyte ions do not get enough time to completely diffuse inside the electrode pores; hence, the capacitance comes mainly from the outer surface of the materials, whereas at the lower scan rate, not only the outer surface Faradaic redox reactions, but also the diffusion processes within the pores contribute to the total capacitance. Therefore, the porosity of the materials may affect the ion diffusion kinetics depending on the pore size which influences the rate capability performance. The BET analysis (Fig. 6a, b) exhibited that the CMO6 composite has higher surface area as well as high pore volume than the pure CuO. Hence, the CMO6 exposes more number of redox-active site to the

electrolyte ions and shows an remarkable performance. Although CMO3 composite has high surface area and pore volume as compared to pure CuO, probably the small pore size of CMO3 makes it barely accessible for the electrolytes ions leading to lower diffusional capacitance of the composite at low scan rate than that in pure CuO.

The total current generated in CV is the combination of diffusion-controlled Faradaic redox current and non-diffusion-controlled capacitive current. These different types of current contribution can be calculated quantitatively using Power law: $i_P = a \, \upsilon^b$ where i_P is the anodic peak current, υ is the scan rate (mV/s), a and b are the adjustable parameters [34]. The value of b gives the idea about the extent of diffusion-controlled Faradaic redox current and non-diffusion-controlled capacitive current. A 0.5 value of b signifies the ideal diffusion-controlled Faradaic redox process, whereas the non-diffusion-controlled capacitive current is expressed by a unit value of
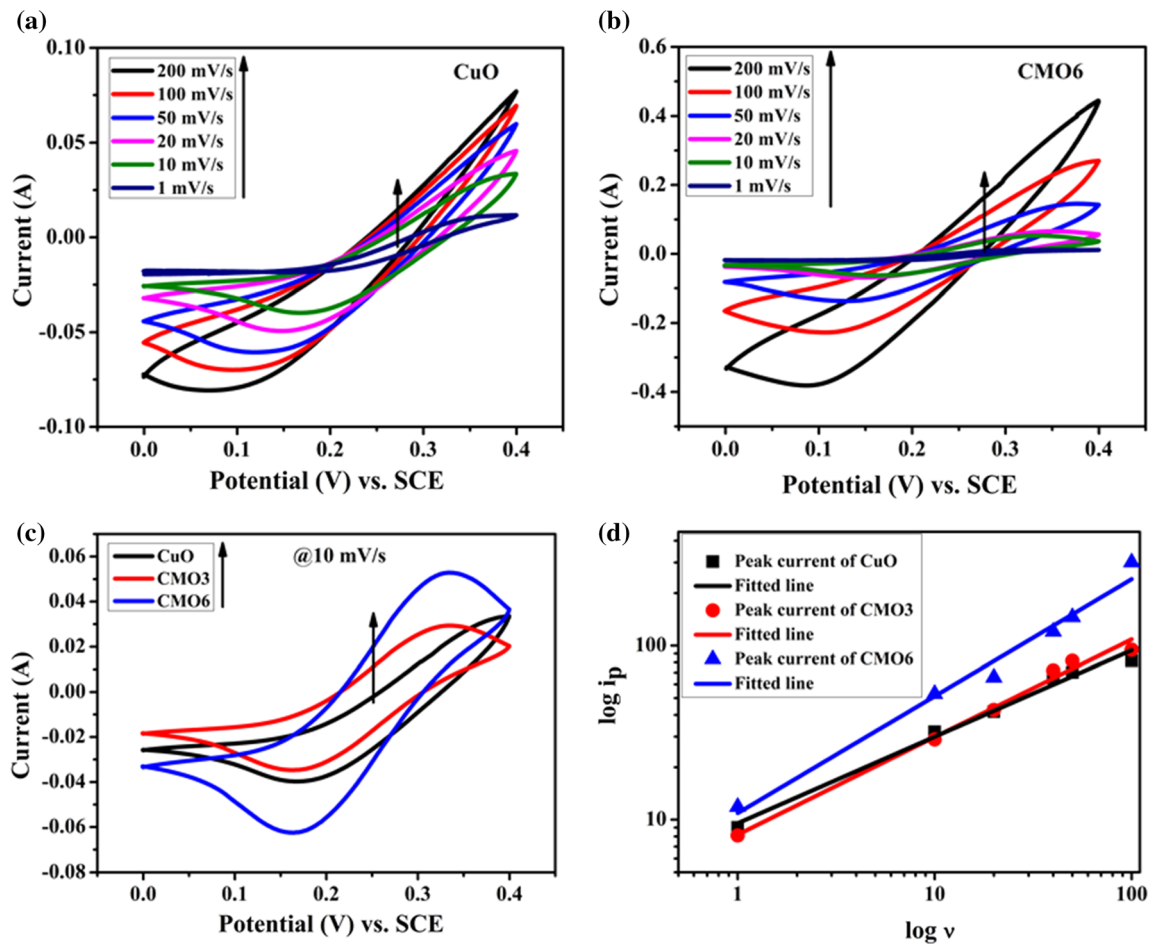
Figure 7 CV plot of CuO (**a**) and CMO6 (**b**) in 2 M KOH containing 0.3 M $K_3[Fe(CN)_6]$ at different scan rates. CV curves of all the materials at a scan rate of 10 mV/s (**c**). Log i_p versus log v plot (**d**) of as-synthesized CuO and CuO–MnO$_2$ composites.

b. The value of b is easily calculated from the slope of the log (i_p) versus log (v) linear curve. From Fig. 7d, the value of b is calculated to be 0.51, 0.56 and 0.67 for CuO, CMO3 and CMO6, respectively, indicating that the capacitances of the electrodes are mainly contributed by diffusion-controlled Faradaic redox charge transfer process.

The galvanostatic charge–discharge (GCD) curves of CuO and CMO6 at various specific currents with a potential window of 0.0–0.4 V in mixed 2 M KOH and 0.3 M $K_3[FeCN_6]$ are shown in Fig. 8a, b. The nonlinear behavior of the discharge curves indicates the Faradaic redox reactions of pseudocapacitive electrodes and the redox-active electrolyte. Furthermore, it is seen that the discharge times are always larger than the charging time at all specific currents, implying the high columbic efficiency of the electrode, which is really promising. The specific capacitance of 2690, 1641, 889, 668 and 539 F/g was

calculated at a specific current of 8, 10, 20, 30 and 50 A/g, respectively, for the CMO6 composite electrode. While the bare CuO achieved the specific capacitance of 2519, 1492.7, 365, 100 and 1 F/g at a specific current of 8, 10, 20, 30 and 50 A/g, respectively. The CMO6 composite shows very high electrochemical performance in redox-mediated electrolyte, which is very high compared to previously reported literature (Table 1).

With increasing the specific current, specific capacitance of both the electrode decreases as the electrons and ions get lower time to diffuse into the electrode at high specific current. Furthermore, with the increase in specific current from 8 to 50 A/g, the capacitance of CuO, CMO3 and CMO6 composites retained 0.04, 7.7 and 20%, respectively (Fig. 8c). So, the CMO6 composite shows better rate capability performance in comparison with the bare CuO and CMO3 composite. Even at high specific current of
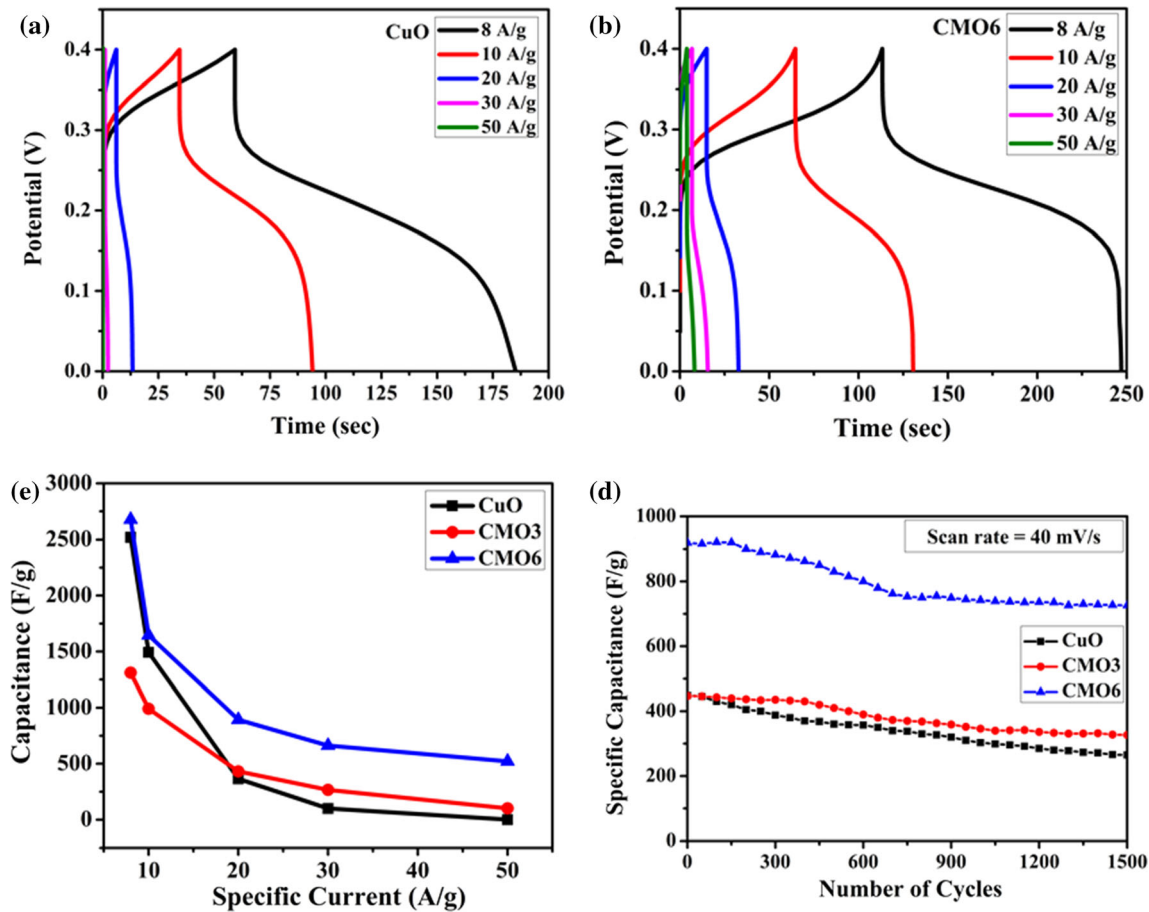
Figure 8 GCD curves of CuO (**a**) and CMO6 composites (**b**) in 2 M KOH containing 0.3 M $K_3[Fe(CN)_6]$ at different specific currents. Capacitance versus specific current plot (**c**) and % change in the specific capacitance versus number of CV cycles (**d**) of as-synthesized CuO, CMO3 and CMO6 composites.

Table 1 Specific capacitance of $CuO–MnO_2$ composite reported earlier

Materials	Capacitance	Specific current	Electrolyte	Reference
$Diatom@CuO@MnO_2$	240 F/g	0.5 A/g	1 M Na_2SO_4	[12]
$Cu/CuO@MnO_2$	177 mF cm^{-2}	0.5 mA/cm^2	1 M KOH	[11]
$CuO@MnO_2$	252.6 F g1	0.1 A/g	1 M Na_2SO_4	[10]
CuO/MnO_2	228 F/g	0.25 A/g	1 M Na_2SO_4	[9]
$CuO@MnO_2$	276 F/g	0.6 A/g	1 M Na_2SO_4	[3]
$CuO–MnO_2$	2690 F/g	8 A/g	2 M KOH + 0.3 M $K_3[Fe(CN)_6]$	This work

50 A/g, it provides high capacitance of 539 F/g, indicating higher stability and better electrochemical performance of the CMO6 electrode. The cycle stability of the as-synthesized materials was studied at a scan rate of 40 mV/s in the same electrolyte, which shows the 59, 73 and 79% capacitance retention after 1500 CV cycles of pure CuO, CMO3 and CMO6 (Fig. 8d), respectively.

The electrochemical impedance spectra were recorded in the frequency range of 200 kHz–0.2 Hz, with sinus amplitude of 10 mV, and expressed in terms of Nyquist plot (Fig. 9) which depicts real and imaginary parts of the complex impedance. The bare CuO nano-needle shows very high magnitude of x-axis (Z_{Re}) intercept, indicating high equivalent series resistance (R_s) than the composite. Further, in the
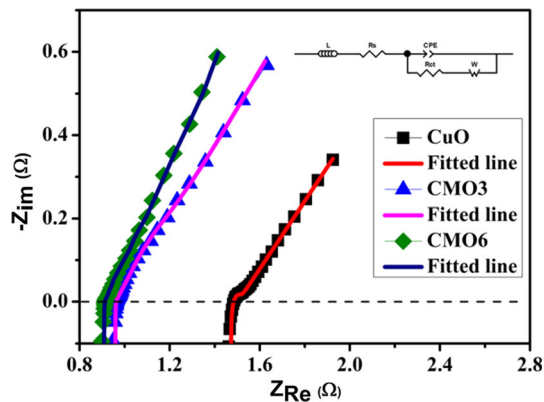
Figure 9 Nyquist plots for CuO and MnO_2–CuO composite (inset: the corresponding equivalent circuit).

high-frequency region, the smaller diameter of the semicircle of the composite implies that it has lower charge transfer resistance (R_{ct}) compared to the bare CuO. The R_s and R_{ct} values of CMO6 composite are lower than the pristine CuO and CMO3 composites [Table S1], suggesting the high electrochemical performance of the CMO6 composite for supercapacitor application.

Conclusions

A simple and cost-effective precipitation approach in combination with conventional hydrothermal method was adopted for fabrication of MnO_2–CuO nanocomposites (CMO3 and CMO6). In the composites, the CuO nano-needles are uniformly covered with MnO_2 nano-sheets. The synthesized materials were characterized using different microscopic and spectroscopic tools. The work beautifully describes a comparative study of the electrochemical behavior of the composites in a redox-mediated electrolyte (0.3 M $K_3[Fe(CN)_6]$ in 2 M KOH). The as-synthesized CMO6 composite with the highest surface area and porosity displays the highest value of capacitance when compared to CuO and CMO3. The CMO6 composite achieved high specific capacitance of 2690 F/g at specific current of 8 A/g with better rate capability. The results of the electrochemical studies imply that the composite CMO6 could be a promising electrode material for supercapacitor application.

Compliance with ethical standards

Conflict of interest The authors declare no conflict of interest.

References

[1] Khare V, Nema S, Baredar P (2016) Solar–wind hybrid renewable energy system: a review. Renew. Sustain. Energy Rev. 58:23–33

[2] Zhang YX, Li F, Huang M (2013) One-step hydrothermal synthesis of hierarchical MnO_2-coated CuO flower-like nanostructures with enhanced electrochemical properties for supercapacitor. Mater. Lett. 112:203–206

[3] Huang M, Zhang Y, Li F et al (2014a) Merging of Kirkendall growth and Ostwald ripening: CuO@MnO_2 core-shell architectures for asymmetric supercapacitors. Sci. Rep. 4:4518

[4] Dubey R, Guruviah V (2019) Review of carbon-based electrode materials for supercapacitor energy storage. Ionics 25:1419–1445

[5] Majumdar D, Mandal M, Bhattacharya SK (2019) V_2O_5 and its carbon-based nanocomposites for supercapacitor applications. ChemElectroChem 6:1623–1648

[6] Mandal M, Ghosh D, Chattopadhyay K et al (2016) A novel asymmetric supercapacitor designed with Mn_3O_4@ multi-wall carbon nanotube nanocomposite and reduced graphene oxide electrodes. J. Electronic. Mater. 45:3491–3500

[7] Ghosh D, Mandal M, Das CK (2015) Solid state flexible asymmetric supercapacitor based on carbon fiber supported hierarchical $Co(OH)_xCO_3$ and $Ni(OH)_2$. Langmuir 31:7835–7843

[8] Mandal M, Ghosh D, Giri S et al (2014) Polyaniline-wrapped 1D $CoMoO_4 \cdot 0.75 H_2O$ nanorods as electrode materials for supercapacitor energy storage applications. RSC Adv. 4:30832–30839

[9] Zhang Z, Ma C, Huang M et al (2015) Birnessite MnO$_2$-decorated hollow dandelion-like CuO architectures for supercapacitor electrodes. J. Mater. Sci. Mater. Electron. 26:4212–4220

[10] Guo XL, Li G, Kuang M, Yu L et al (2015) Tailoring kirkendall effect of the KCu$_7$S$_4$ microwires towards CuO@MnO$_2$ core-shell nanostructures for supercapacitors. Electrochim. Acta 174:87–92

[11] Wang X, Chen C, Chen K et al (2016) MnO$_2$ nanosheets-decorated CuO nanoneedles arrays@ Cu foils for supercapacitors. Int. J. Electrochem. Sci. 11:3425–3435

[12] Zhang Y, Guo WW, Zheng TX et al (2018) Engineering hierarchical Diatom@ CuO@ MnO$_2$ hybrid for high performance supercapacitor. Appl. Surf. Sci. 427:1158–1165

[13] Chen Q, Heng B, Wang H et al (2015) Controlled facile synthesis of hierarchical CuO@MnO$_2$ core–shell nanosheet arrays for high-performance lithium-ion battery. J. Alloys Compd. 641:80–86

[14] Zeng C, Gao C, Yuan L et al (2017) Water evaporation-induced self-assembly of hierarchical CuO/MnO$_2$ composite nanospheres and their applications in lithium-ion batteries. NANO 12:1750022

[15] Yang Z, Yang Y, Zhu X et al (2014) An outward coating route to CuO/MnO$_2$ nanorod array films and their efficient catalytic oxidation of acid fuchsin dye. Ind. Eng. Chem. Res. 53:9608–9615

[16] Pal J, Mondal C, Sasmal AK et al (2014) Account of nitroarene reduction with size-and facet-controlled CuO–MnO$_2$ nanocomposites. ACS Appl. Mater. Interfaces 6:9173–9184

[17] Luo X, Liang H, Qu F et al (2018) Free-standing hierarchical α-MnO$_2$@CuO membrane for catalytic filtration degradation of organic pollutants. Chemosphere 200:237–247

[18] Norsic C, Tatibouët JM, Batiot-Dupeyrat C et al (2018) Methanol oxidation in dry and humid air by dielectric barrier discharge plasma combined with MnO$_2$–CuO based catalysts. Chem. Eng. J. 347:944–952

[19] Qian K, Qian Z, Hua Q et al (2013) Structure–activity relationship of CuO/MnO$_2$ catalysts in CO oxidation. Appl. Surf. Sci. 273:357–363

[20] Prathap MA, Sun S, Wei C et al (2015) A novel non-enzymatic lindane sensor based on CuO–MnO$_2$ hierarchical nano-microstructures for enhanced sensitivity. Chem. Commun. 51:4376–4379

[21] Bhuvaneshwari S, Papachan S, Gopalakrishnan N (2017) Free standing CuO-MnO$_2$ nanocomposite for room temperature ammonia sensing. AIP Conf. Proc. 1832:050126

[22] Wessells CD, Huggins RA, Cui Y (2011) Copper hexacyanoferrate battery electrodes with long cycle life and high power. Nat. Commun. 2:1–5

[23] Aruchamy K, Nagaraj R, Manohara HM et al (2020) One-step green route synthesis of spinel ZnMn$_2$O$_4$ nanoparticles decorated on MWCNTs as a novel electrode material for supercapacitor. Mater. Sci. Eng. B 252:114481

[24] Subramani K, Jeyakumar D, Sathish M (2014) Manganese hexacyanoferrate derived Mn$_3$O$_4$ nanocubes–reduced graphene oxide nanocomposites and their charge storage characteristics in supercapacitors. Phys. Chem. Chem. Phys. 16:4952–4961

[25] Huang M, Zhang Y, Li F et al (2014b) Facile synthesis of hierarchical Co$_3$O$_4$@ MnO$_2$ core–shell arrays on Ni foam for asymmetric supercapacitors. J. Power Sources 252:98–106

[26] Kliche G, Popovic ZV (1990) Far-infrared spectroscopic investigations on CuO. Phys. Rev. B 42:10060

[27] Ethiraj AS, Kang DJ (2012) Synthesis and characterization of CuO nanowires by a simple wet chemical method. Nanoscale Res. Lett. 7:70

[28] Chen L, Li L, Li G (2008) Synthesis of CuO nanorods and their catalytic activity in the thermal decomposition of ammonium perchlorate. J. Alloys Compd. 464:532–536

[29] Zhao B, Liu P, Zhuang H et al (2013) Hierarchical self-assembly of microscale leaf-like CuO on graphene sheets for high-performance electrochemical capacitors. J. Mater. Chem. A 1:367–373

[30] Khan R, Vaseem M, Jang L et al (2014) Low temperature preparation of CuO nanospheres and urchin-shaped structures via hydrothermal route. J. Alloys Compd. 609:211–214

[31] Zheng L, Liu X (2007) Solution-phase synthesis of CuO hierarchical nanosheets at near-neutral pH and near-room temperature. Mater. Lett. 61:2222–2226

[32] Huang M, Zhang Y, Li F et al (2014c) Self-assembly of mesoporous nanotubes assembled from interwoven ultrathin birnessite-type MnO$_2$ nanosheets for asymmetric supercapacitors. Sci. Rep. 4:3878

[33] Tang B, Wang G, Zhuo L et al (2006) Novel dandelion-like beta-manganese dioxide microstructures and their magnetic properties. Nanotechnology 17:947

[34] Ray A, Roy A, Saha S et al (2019) Electrochemical energy storage properties of Ni-Mn-oxide electrodes for advance asymmetric supercapacitor application. Langmuir 35:8257–8267